

Review

# Atomic Layer Deposition of Inorganic Films for the Synthesis of Vertically Aligned Carbon Nanotube Arrays and Their Hybrids

Guang-Jie Yuan <sup>1</sup>, Jie-Fei Xie <sup>2</sup>, Hao-Hao Li <sup>2</sup>, Hong-Liang Lu <sup>3</sup>  and Ying-Zhong Tian <sup>1,\*</sup> 

<sup>1</sup> Shanghai Key Laboratory of Intelligent Manufacturing and Robotics, School of Automation and Mechanical Engineering, Shanghai University, Shanghai 200444, China; guangjie@shu.edu.cn

<sup>2</sup> SMIT Center, School of Automation and Mechanical Engineering, Shanghai University, Shanghai 201800, China; okxjf@shu.edu.cn (J.-F.X.); lihaoer@i.shu.edu.cn (H.-H.L.)

<sup>3</sup> State Key Laboratory of ASIC and System, School of Microelectronics, Fudan University, Shanghai 200433, China; honglianglu@fudan.edu.cn

\* Correspondence: troytian@shu.edu.cn

Received: 6 November 2019; Accepted: 28 November 2019; Published: 1 December 2019



**Abstract:** Vertically aligned carbon nanotube arrays (VACNTs) have many excellent properties and show great potential for various applications. Recently, there has been a desire to grow VACNTs on nonplanar surfaces and synthesize core-sheath-structured VACNT–inorganic hybrids. To achieve this aim, atomic layer deposition (ALD) has been extensively applied, especially due to its atomic-scale thickness controllability and excellent conformality of films on three-dimensional (3D) structures with high aspect ratios. In this paper, the ALD of catalyst thin films for the growth of VACNTs, such as  $\text{Co}_3\text{O}_4$ ,  $\text{Al}_2\text{O}_3$ , and  $\text{Fe}_2\text{O}_3$ , was first mentioned. After that, the ALD of thin films for the synthesis of VACNT–inorganic hybrids was also discussed. To highlight the importance of these hybrids, their potential applications in supercapacitors, solar cells, fuel cells, and sensors have also been reviewed.

**Keywords:** ALD; VACNTs; core-sheath structure; VACNT–inorganic hybrids

## 1. Introduction

Vertically aligned carbon nanotube arrays (VACNTs) have good alignment, high specific surface areas, excellent electrical and thermal conductivity, superior mechanical properties, high purity, low expansion coefficients, low weights, and antiaging and antioxidation properties [1–5]. Due to their outstanding properties, VACNTs show great potential for a wide variety of applications, such as field emitters for display, biological sensors, energy storage devices, and thermal interface materials [6–13]. Generally, VACNTs are usually made by carbon-arc discharge, laser ablation of carbon, or chemical vapor deposition (CVD) typically on catalytic particles [14]. Compared with the others, CVD is low-cost, controllable, and suitable for mass preparation, so it has been the most important and common method to synthesize the VACNTs [15]. Currently, many researchers focus on the synthesis of high-quality VACNTs with the optimization of different parameters of catalyst and buffer layers, such as roughness and stoichiometry [16]. Furthermore, the growth of VACNTs on nonplanar substrates is increasingly important due to their particular applications, such as fuel cell electrodes. Generally, they consist of a carbon nanofiber or porous matrix, and it is desirable to make hierarchical structures by growing VACNTs onto the nanofibers or porous structures [17–20]. In addition, compared with a planar surface, a nonplanar surface can largely increase the specific surface area, which would be very beneficial for the preparation and further applications of VACNTs [21–23]. To synthesize high-quality VACNTs on nonplanar surfaces, it is very important to deposit uniform catalysts on them, especially for three-dimensional (3D) structures with high aspect ratios.

In recent years, core-sheath-structured VACNT–inorganic hybrids have become critical due to their potential applications in supercapacitors, solar cells, fuel cells, and sensors [24–30]. Combining VACNTs with multifunctional inorganic nanomaterials can take advantage of the synergistic effects between the VACNT–inorganic interface, and it is expected to bring superior combined properties to the hybrids [31]. Generally, for many applications of VACNT–inorganic hybrids, the performance of the devices crucially depends on the thickness and conformality of the inorganic thin films of the VACNTs [32]. However, due to the high aspect ratio of VACNTs, it is a challenge to obtain conformal and uniform coatings on them.

To deposit uniform thin films on nonplanar substrates, especially for 3D structures and VACNTs with high aspect ratios, the traditional physical vapor deposition (PVD) and CVD methods are not very suitable due to their relatively limited step coverage [33]. Unlike these methods, atomic layer deposition (ALD) can achieve pinhole-free, dense, and conformal thin films on 3D structures with high aspect ratios with atomic scale precision due to its self-limited behavior, as shown in Figure 1a,b [34–37]. Therefore, ALD is a promising technology for the uniform deposition of catalysts on 3D structures with a high aspect ratio and the conformal inorganic coating of VACNTs. Recently, some researchers have widely used ALD to deposit inorganic films on some 3D structures with the high aspect ratio, such as membranes [38,39]. Compared with membranes, VACNTs also have the high aspect ratio, but they are theoretically more difficult to be coated by ALD, due to chemically inert graphitic surfaces of the pristine VACNTs [32]. Figure 2 illustrates the number of publications involving the ALD of inorganic films for the synthesis of VACNTs and their hybrids in the last 10 years. Despite there have some reviews about ALD of inorganic films on carbon nanotubes (CNTs), comprehensive reviews are not available about ALD of inorganic films on VACNTs and for their growth [40]. The main goal of this work is to provide a brief overview of fundamentals of ALD, and discuss the current research progress about ALD of inorganic films for the synthesis of VACNTs and their hybrids through existing publications.

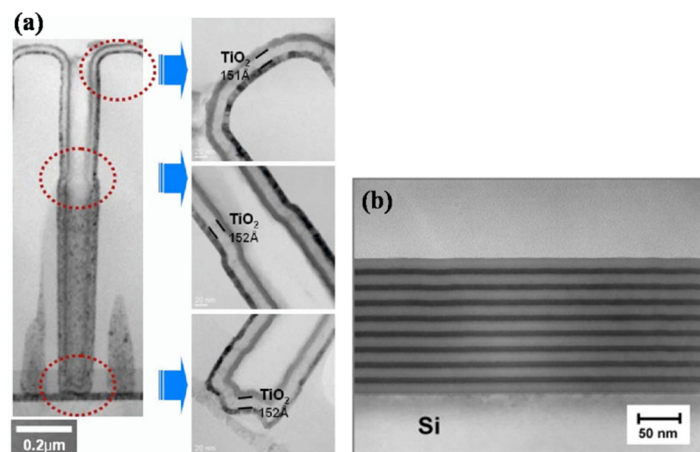


**Figure 1.** (Color online) Properties of atomic layer deposition (ALD)-grown films: (a) Uniform thickness inside narrow holes [41]. (Copyright 2007 Electrochemical Society, Inc.) Adapted with permission from Electrochemical Society. Permission to reuse must be obtained from the copyright holder. (b) Atomic level control composition [42]. Adapted with permission from Elsevier. Copyright 2005 Elsevier.

The structure of this review is organized in the following manner. Firstly, the significance of ALD is introduced for the growth of VACNTs on nonplanar surface and the synthesis of core-sheath-structured VACNT–inorganic hybrids in Section 1. In Section 2, the fundamentals of ALD are mentioned, such as “ALD window”. In Section 3, ALD of catalyst thin films for the synthesis of VACNTs is discussed. Finally, ALD for the inorganic coating of VACNTs is also discussed for the applications of supercapacitors, solar cells, fuel cells, and sensors in Section 4.

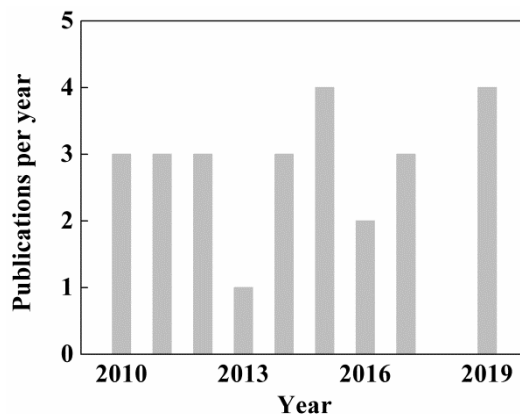


**Figure 2.** (Color online) Number of publications per year with respect to ALD of inorganic films for the synthesis of vertically aligned carbon nanotube arrays (VACNTs) and their hybrids in the last ten years.

## 2. Fundamentals of ALD

ALD can be defined as a film deposition technique that is based on the sequential use of self-terminating reactions [43]. The basic principle of the ALD cycle is shown in Figure 3. First, the precursors are adsorbed on the surface in the precursor feeding period, and the adsorption process is theoretically self-limited. Second, the unadsorbed precursors are removed by a purge period using  $N_2$  or Ar. After that, the reactants, such as  $H_2$ ,  $O_2$ , and  $NH_3$ , react with the adsorbed precursors in the reactant feeding period, and a self-terminating reaction happens between them. Finally, the remaining reactants and gaseous reaction by-products are removed by another purge period. Each ALD cycle adds a given amount of material to the surface, which is referred to as the growth per cycle (GPC) [43,44]. Generally, ALD cycles need be optimized to achieve deposition of a film with the desired thickness [43]. The self-limiting adsorption and reaction show that ALD is a surface-controlled process, and the GPC is usually measured to confirm its self-limiting growth as a function of precursor and reactant feeding period. Because of the self-limiting behavior, ALD-grown films are pinhole-free, have excellent conformality, and are uniform with atomic scale precision [41,42].

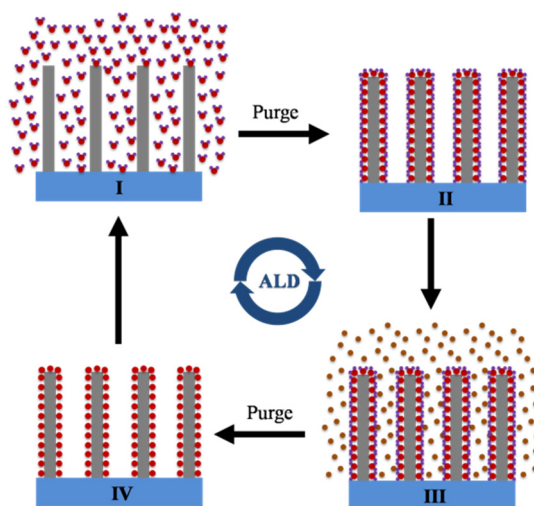


**Figure 3.** (Color online) Schematic representation of one ALD cycle on the VACNTs, including four steps: (I) Exposure of the precursors, (II) a purge period, (III) exposure of the reactants, and (IV) a purge period. (Adapted from ref. [32]).

Theoretically, the alternating purging is almost distinctive as the self-limiting growth mechanism of one monolayer in the ALD process [43]. However, in the vast majority of cases, only a fraction of a

monolayer may be achieved in each cycle, which is related to some factors, including physisorbed precursors, steric hindrance between the ligands, limitations of the activation energy of surface reactions, and decomposition and desorption of surface species [45–51]. Among the parameters available in controlling these factors as mentioned above, the deposition temperature is most important in the ALD process. Generally, “ALD window” can be defined as a temperature range where the GPC is nearly constant, allowing for reliable and repeatable results despite slight temperature variation, as shown in Figure 4 [43,52–54]. As shown in region 1 of Figure 4, GPC decreases as the deposition temperature increases due to the physisorption of precursors. As a result, precursors condense, and their adsorption forms multilayers [55,56]. Generally, adsorption can be divided into two general classes based on the strength of the interaction between the adsorbing molecules and the solid surface. One class is physisorption (i.e., physical adsorption), and the other is chemisorption (i.e., chemical adsorption) [57,58]. In general, chemisorption involves the making and optional breaking of chemical bonds between the adsorbing molecules and the surface [59]. Therefore, the surface only accepts one layer, and adsorption forms a monolayer of the adsorbed molecules. However, physisorption originates from weak interactions (van der Waals force), and minimal changes typically occur in the structure of the adsorbing molecules [60]. With physisorption, the interactions are not specific to the molecule/surface pair, so adsorption may form multilayers. Because of physisorption, ALD is sometimes not self-limited to form a monolayer, but a multilayer forms in each cycle. In region 2, GPC increases with increasing temperature, which can be explained by the reducing effect of the steric hindrance of the precursor ligands or the activation of the reaction between precursors and reactants [61–64]. Steric hindrance of the ligands can cause the ligands of the adsorbed molecules (precursors) to shield part of the surface from being accessible to the other precursor molecules, which limits the surface density of adsorbed precursors [65]. It may restrict the total number of adsorbed precursors on the surface and limit the GPC of ALD films [45]. On the other hand, surface reactions may not be activated between the adsorbed precursors and the reactants at the low deposition temperature, which also limits the GPC [41]. In region 3, GPC increases as the temperature increases due to the decomposition of precursors on their own during the ALD cycle. Decomposition of the surface species may occur even at the minimum temperature required for the surface reactions, which makes the ALD process not self-limiting and the process tends to CVD mode [43,66]. In region 4, GPC decreases with increasing temperature due to desorption of the precursors on the surface [45]. Due to these effects, the ideal model for ALD, the self-limiting growth mechanism of one monolayer, cannot always be achieved in some ALD processes.

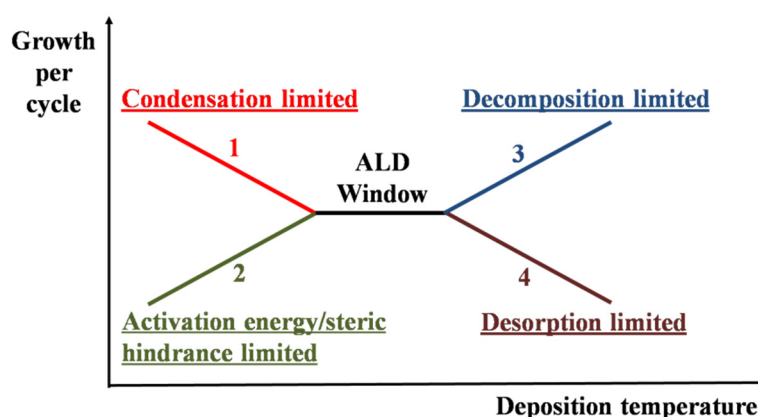


**Figure 4.** (Color online) Schematic of ALD window: Possible behavior for the growth per cycle (GPC) versus deposition temperature [43]. Copyright 2010 American Chemical Society.

### 3. ALD of Catalyst Thin Films for the Synthesis of VACNTs

Generally, the CVD method can be used to synthesize VACNTs on predefined sites of a patterned substrate and has good control of the growth parameters, so it has been extensively used for the

growth of VACNTs [67–72]. Uniform catalysts are critical to the growth of high-quality VACNTs on substrates using CVD, especially for the growth of single-walled VACNTs [73]. Furthermore, there are increasing demands for the growth of VACNTs on nonplanar substrates, so it is quite important to achieve conformal catalysts on these 3D structures [16,74]. Currently, ALD has been widely used to form uniform catalysts on planar and nonplanar structures for the growth of VACNTs due to its atomic-level precision and excellent conformality.

Generally, there is a key requirement for growing single-walled VACNTs using extremely small catalyst nanoparticles, typically approximately one to several nanometers [75]. Commonly, a few monolayers of inorganic films are first deposited and subsequently annealed to form catalyst nanoparticles [76,77]. However, uniform and reproducible deposition of such ultrathin films using traditional PVD is challenging, with complications such as sputtering and evaporation. Recently, many researchers have used ALD to form uniform and ultrathin catalyst films for the growth of single-walled VACNTs [75,78]. In 2017, Thissen et al. used plasma-enhanced ALD (PE-ALD) to deposit a  $\text{Co}_3\text{O}_4$  thin film using cobaltocene ( $\text{CoCp}_2$ ) and  $\text{O}_2$  [75]. After annealing in the  $\text{H}_2/\text{Ar}$  flow, the  $\text{Co}_3\text{O}_4$  film was reduced to metallic Co catalyst nanoparticles. Finally, atmospheric pressure CVD (APCVD) was applied to successfully synthesize the single-walled VACNTs using ethanol and  $\text{H}_2$ . Tang et al. also reported that single-walled VACNTs could grow directly on ALD  $\text{Al}_2\text{O}_3$  catalyst nanoparticles [78]. A 1 nm  $\text{Al}_2\text{O}_3$  film was deposited on a sapphire substrate by ALD using trimethylaluminum (TMA) and  $\text{H}_2\text{O}$ . After annealing at 1100 °C in air for 10 h, the  $\text{Al}_2\text{O}_3$  film was converted to catalyst nanoparticles. Finally, APCVD was used to successfully synthesize single-walled VACNTs using ethanol and  $\text{H}_2$ .

Recently, for the synthesis of VACNTs on nonplanar substrates, floating catalyst chemical vapor deposition (FC-CVD) has been widely used, and the catalyst nanoparticles directly formed on 3D structures by the decomposition of catalyst precursors [21,79]. However, the sizes of catalyst nanoparticles were difficult to control during the FC-CVD process. The nanoparticles easily agglomerated into large particles, which generally resulted in large-diameter multiwalled VACNTs with limited specific surface areas [21,80]. To overcome this obstacle, many researchers have used ALD to deposit uniform and ultrathin catalyst films on nonplanar substrates. Subsequently, uniform catalyst nanoparticles could be achieved with the annealing process for the growth of VACNTs on these substrates [80,81]. In 2010, Zhou et al. used ALD to deposit an  $\text{Fe}_2\text{O}_3$  film on 3D quartz fibers using acetylacetonate ( $\text{Fe}(\text{acac})_3$ ) and ozone ( $\text{O}_3$ ) [80]. After deposition, the  $\text{Fe}_2\text{O}_3$  film was transferred into the CVD chamber and reduced to Fe catalyst nanoparticles with annealing under the protection of Ar and  $\text{H}_2$ . Finally,  $\text{C}_2\text{H}_4$  and  $\text{CO}_2$  were introduced into the chamber, and the multiwalled VACNTs grew radially and self-organized into leaf-like structures on quartz fibers [80]. Recently, Chen et al. used ALD to deposit iron oxide films on a porous alumina ( $\text{Al}_2\text{O}_3$ ) foam using tert-butylferrocene ( $\text{C}_{14}\text{H}_{18}\text{Fe}$ ) and  $\text{O}_3$  [81]. Generally,  $\text{Al}_2\text{O}_3$  foams were 3D structures and contained interconnected open pores, as shown in Figure 5a. To grow the VACNTs at the top and inside surface of the pores, ALD was used to deposit iron oxide films on both the top and inside of the foam surface. After that, the samples were subjected to annealing under  $\text{H}_2$  atmosphere, and the iron oxide films were converted to Fe catalyst nanoparticles. Finally, low-pressure CVD (LPCVD) was used to successfully synthesize the VACNTs on whole surfaces of the porous  $\text{Al}_2\text{O}_3$  foam using acetylene ( $\text{C}_2\text{H}_2$ ) and  $\text{H}_2$ , as shown in Figure 5b,c. Figure 5d shows that the VACNTs were double-walled inside the foam, similar to those grown on planar  $\text{Al}_2\text{O}_3$  substrates [81].

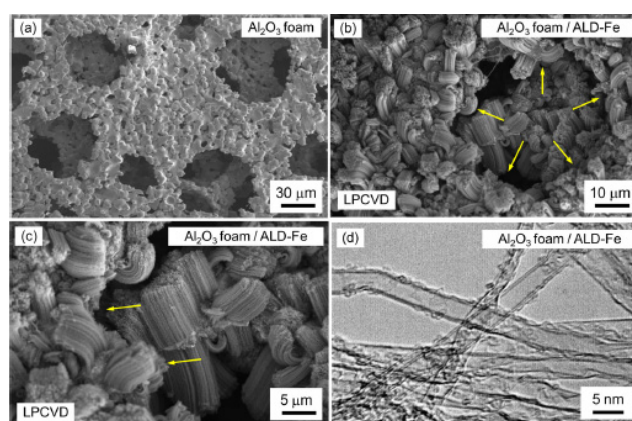


**Figure 5.** (Color online) (a) SEM images of the as-received  $\text{Al}_2\text{O}_3$  foam; (b,c) low- and high-magnification SEM images of VACNTs inside the foam surface; (d) HRTEM image of the VACNTs. The VACNTs grow from inside the foam (as indicated by arrows) [81]. Copyright AIP Publishing 2014

#### 4. ALD for the Inorganic Coating of VACNTs

Recently, VACNT–inorganic hybrids have attracted much attention due to their potential applications, such as supercapacitors, solar cells, fuel cells, and sensors [82,83]. Compared to the individual constituents, the properties of VACNT–inorganic hybrids, such as the optical and electrical properties, could apparently be enhanced [84]. However, it was challenging to deposit inorganic thin films on VACNTs due to their complex surface and topology [32]. Theoretically, due to chemically inert graphitic surfaces of the pristine VACNTs, no bonding sites could be supplied for the nucleation of inorganic films, which prevented the conformal coating of VACNTs [85–90]. In practice, however, there was a sufficient density of surface defect sites of the CVD-grown VACNTs, and these surface defect sites allowed nucleation of the inorganic films along the surface of the VACNTs [32]. The inorganic film then grew from these nucleation sites and finally merged to form a continuous film [91–93]. However, to reach a state of complete coverage, a relatively large number of ALD cycles were required, which depended on the density of defect sites. Generally, 50–100 ALD cycles were required for the deposition of a conformal inorganic film on CVD-grown VACNTs [32]. Second, the vertically aligned nature of the VACNTs also presented a challenge for achieving conformal and uniform inorganic films on them [32]. As shown in Figure 3, VACNTs had high aspect ratios and large surface areas, and in high surface area structures, such a high aspect ratio requires higher precursor dosing, for reaching the saturation of a larger surface. In parallel, high aspect ratio structures demand (i) longer diffusion times to attain saturation of the whole surface and thus uniform coating; and (ii) longer purging times to ensure the proper elimination from the ALD chamber of unreacted precursor molecules and by-products to avoid any undesirable gas reaction between the precursors [41].

In the last decade, many researchers have focused on the deposition of uniform and conformal inorganic films on VACNTs [31,83,94]. In 2010, Li et al. directly used ALD to deposit continuous and uniform ZnO thin films on multiwalled VACNTs using diethylzinc ( $\text{Zn}(\text{C}_2\text{H}_5)_2$ , DEZ) and  $\text{H}_2\text{O}$  [83]. The deposited ZnO films had good crystalline quality, and VACNT–inorganic hybrids were successfully synthesized. In 2011, Min et al. also directly used ALD to form crystalline ZnO nanoparticles on single-walled VACNTs using DEZ and  $\text{H}_2\text{O}$  [94]. The nanoparticles were fairly spherical, and their size was considerably uniform [94]. Although inorganic films could be formed directly on VACNTs in some cases, the defect density was relatively high on the walls of VACNTs, which acted as nucleation sites for the deposition of inorganic films [87,95–97]. However, VACNTs with large numbers of defects are highly undesirable for many applications because the high defect density limits their physical properties [31]. Although VACNTs with high purity and a low defect density could be synthesized, their surfaces were nonreactive and chemically inert toward the ALD precursor molecules, which could not readily nucleate the growth of conformal organic thin films [98,99]. This resulted in sparse

nucleation and the development of a bead-like structure on the surface of VACNTs instead of a uniform coating [100]. To overcome this issue, covalent and noncovalent functionalization processes have generally been developed to promote interactions between the surface of VACNTs and precursor molecules [31,101]. In 2014, Stano et al. successfully deposited conformal alumina ( $\text{Al}_2\text{O}_3$ ) films on functionalized multiwalled VACNTs by ALD using trimethylaluminum ( $(\text{CH}_3)_3\text{Al}$ , TMA) and  $\text{H}_2\text{O}$  [31]. Before the deposition of the  $\text{Al}_2\text{O}_3$  films, the surfaces of the VACNTs were modified through some posttreatments, such as pyrolytic carbon deposition, high-temperature thermal annealing, and oxygen plasma functionalization [31]. The post-treatments apparently increased the defect density on the walls of the VACNTs, and core-sheath-structured VACNT- $\text{Al}_2\text{O}_3$  hybrids were achieved. Compared with the pristine VACNTs, the hybrids had better compressive properties and thermal stability to oxidation. In 2017, Li et al. also used ALD to deposit conformal  $\text{TiO}_2$  films on functionalized multiwalled VACNTs using tetrakis(dimethylamino)titanium ( $\text{Ti}(\text{N}(\text{CH}_3)_2)_4$ , TDMAT) and  $\text{H}_2\text{O}$  [101]. Many hydroxyl ( $>\text{COH}$ ) and carboxyl ( $-\text{COOH}$ ) groups attached to the surface of VACNTs could serve as nucleation sites for the subsequent  $\text{TiO}_2$  deposition [102,103]. The core-sheath-structured VACNT- $\text{TiO}_2$  hybrids were successfully achieved using ALD. Compared with pristine VACNTs, the hybrid structures had tensile strengths that varied slightly, but their electrical conductivity was reduced by 28.3% with 715 ALD cycles [101]. Generally, besides the conformality of deposited inorganic films on VACNTs, their electrical properties are also critical, such as electrical conductivity. To further improve the electrical conductivity of inorganic films, some reactive gas can be used to reduce the impurities in the deposited films, such as carbon. Therefore, ALD of high-purity and conformal inorganic films on VACNTs is supposed to be developed in the future.

#### 4.1. Supercapacitors

According to different charge storage mechanisms, there are mainly two kinds of supercapacitors, electrical double layer capacitors (EDLCs) and pseudocapacitors [104]. EDLCs store electrical charges at the electrode–electrolyte interface, and the number of ions gathering at the surface is proportional to the surface area of the electrodes [105–107]. Therefore, the energy storage capabilities of electrodes can be increased by increasing the electrode surface area, which were commonly achieved by using high-surface-area materials with high intrinsic capacitances, such as VACNTs, porous carbon, and activated carbon [108,109]. Compared with these materials, the VACNTs had better capacitive performances, higher specific areas, higher life-cycle stability, and more uniform pore sizes that simplified the choice of electrolyte species [110–112]. For pseudocapacitors, charge storage is based on charge transfer between the electrode and electrolyte, and their charge storage is achieved by a faradaic redox reaction at the surfaces of the electrodes [104,113]. If these two mechanisms occur at the same time, the charge storage capacity of the supercapacitor could be dramatically increased, so both large-surface-area electrodes and highly active pseudocapacitive materials have been used to achieve high supercapacitor performance [113].

Recently, many core-sheath-structured VACNT–inorganic hybrids have already been developed to enhance the charge storage capacity of supercapacitors [104,113–115]. In 2011, Pint et al. used ALD to deposit conformal  $\text{Al}_2\text{O}_3$  and Al-doped ZnO (AZO) films on functionalized single-walled VACNTs for the fabrication of supercapacitors [114]. TMA and  $\text{H}_2\text{O}$  were used for ALD of  $\text{Al}_2\text{O}_3$  films as the precursors and reactants, respectively. AZO films were formed by using alternating layers of  $\text{Al}_2\text{O}_3$  and ZnO that were synthesized by DEZ and  $\text{H}_2\text{O}$ . Core-sheath-structured AZO/ $\text{Al}_2\text{O}_3$ /VACNT hybrids were successfully achieved, and the developed supercapacitor architectures have much higher energy densities with similar power densities, comparable to conventional solid-state capacitor devices [114]. In 2015, Fiorentino et al. used ALD to directly form conformal  $\text{Al}_2\text{O}_3$  and titanium nitride (TiN) layers on multiwalled VACNTs, and core-sheath-structured TiN/ $\text{Al}_2\text{O}_3$ /VACNT hybrids were synthesized to enhance the supercapacitor performances [104]. TMA and  $\text{H}_2\text{O}$  were used for ALD of  $\text{Al}_2\text{O}_3$ , and  $\text{TiCl}_4$  and  $\text{NH}_3$  were used for ALD of TiN. Compared to the capacitance of a planar device with the same footprint, the hybrids increased the effective capacitance by a factor of

4.2–5 [104]. In 2015, Fisher et al. applied ALD to directly deposit conformal and uniform titanium oxide ( $\text{TiO}_2$ ) on multiwalled VACNTs using TDMAT and  $\text{H}_2\text{O}$  [115]. The core-sheath-structured  $\text{TiO}_2/\text{VACNT}$  hybrids introduced pseudocapacitive charge storage properties to the electrodes, which utilized both of the charge storing mechanisms mentioned above. The hybrids apparently improved the performances of the supercapacitors with an improvement in the specific capacitance, power, and energy [115]. In 2015, Warren et al. used ALD to directly deposit conformal ruthenium oxide ( $\text{RuO}_x$ ) on VACNTs using bis(ethylcyclopentadienyl)ruthenium(II) ( $\text{Ru}(\text{EtCp})_2$ ) and oxygen ( $\text{O}_2$ ) [116]. Core-sheath-structured  $\text{RuO}_x/\text{VACNT}$  hybrids were successfully synthesized, which had fast, reversible redox reactions and exceptional life cycle performance. Compared with bare VACNT electrodes, the hybrids achieved higher specific capacitances [116]. In 2016, Kao et al. used PEALD to form conformal TiN films on multiwalled VACNTs using TDMAT and  $\text{N}_2$ , as shown in Figure 6 [113]. After that, the surface layer of TiN oxidized and formed a native oxide layer of  $\text{TiO}_{2-x}\text{N}_x$ , which had a high nitrogen concentration and a large number of oxygen vacancies for enhancing energy storage capabilities through pseudocapacitance. The storage and release of electrical charges occurred by adsorption and desorption of charges on the surface of TiN and oxidation of the surface layer [113]. The core-sheath-structured  $\text{TiO}_{2-x}\text{N}_x/\text{TiN}/\text{VACNT}$  hybrids increased the capacitance by increasing the surface area and by the pseudocapacitive effect, and over 500% enhancement of capacitance was achieved compared with that of the bare VACNT electrodes [113]. Therefore, the core-sheath-structured VACNT–inorganic hybrids are promising to be the electrodes of the supercapacitors, and largely enhance their charge storage capacity.

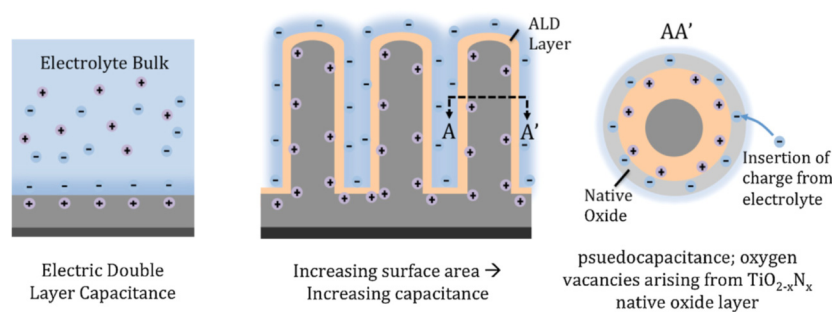


**Figure 6.** (Color online) Conceptual illustrations of improving capacitance through increased surface area and the pseudocapacitive effect [113]. Copyright Elsevier 2016.

#### 4.2. Solar Cells

In the past decade, many researchers have focused on the development of devices that convert sunlight into usable sources of energy and the improvement of solar cell performance [117,118]. 3D architectures have been widely used to enhance the carrier collection efficiency and photo management of solar devices [118–121]. The overall conversion efficiency of these materials could be improved by orthogonalizing the light absorption and carrier collection processes, reducing surface reflectance, and enhancing absorption [122]. Generally, 3D solar devices have been fabricated using textured substrates and/or back-contacts followed by the deposition of thin films [123]. Currently, VACNTs are widely used for the back-contacts of 3D solar devices due to their high surface area, excellent electrical properties, and good catalytic properties [124,125]. Some researchers have also focused on the fabrication of VACNT–inorganic hybrids to improve the performance of solar cells [126,127]. In 2011, Pint et al. used ALD to deposit conformal  $\text{TiO}_2$  films on functionalized and texturized VACNTs using titanium(IV) isopropoxide ( $\text{Ti}(\text{OCH}(\text{CH}_3)_2)_4$ , TTIP) and  $\text{H}_2\text{O}$ , as shown in Figure 7a [126]. Core-sheath-structured VACNT– $\text{TiO}_2$  hybrids were successfully fabricated. As shown in Figure 7b, the high-aspect-ratio structurally texturized VACNT electrodes had a semiconductor absorber with a normal vector oriented at some angle larger than  $60^\circ$ . The effective thickness of the semiconductor was significantly greater than the actual physical thickness, and more photons could be absorbed closer to a point where they could be collected [126]. The short circuit current density ( $J_{\text{SC}}$ ) for the  $\text{TiO}_2/\text{VACNT}$  solar cell was 3

times higher than that of the planar counterpart, which could be explained by a combination of reduced reflectance, enhanced adsorption due to an increased effective optical path length, and enhanced carrier collection efficiency [126]. In 2019, Yun et al. also used ALD to directly deposit Ru films on multiwalled VACNTs using Ru(EtCp)<sub>2</sub> and O<sub>2</sub> [127]. Unlike the core-sheath structure, Ru films directly connected VACNTs in the top-surface region by acting as their bridges without destroying their microporous structure. The results showed that the VACNT-Ru hybrids could apparently decrease the resistance of as-synthesized VACNTs, which improved the performance of the prepared solar cells [127]. Compared with the traditional solar cells, VACNTs-based 3D solar devices are very likely to be used for the improvement of the overall conversion efficiency.

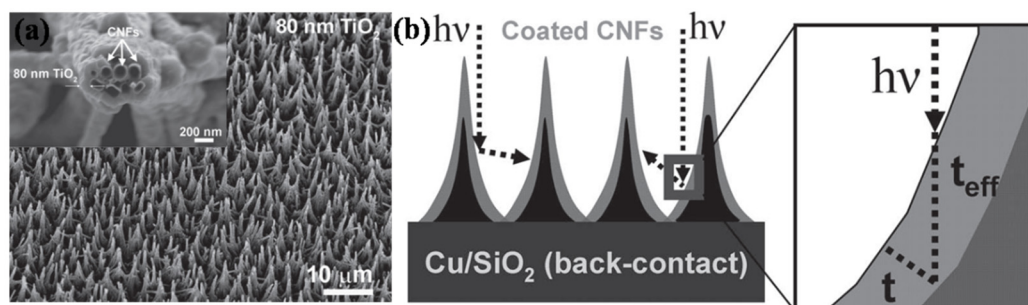


**Figure 7.** (Color online) (a) SEM images of textured VACNTs coated with TiO<sub>2</sub> thin films and (b) scheme illustration of the antireflective nature of a highly 3D structure [126]. Copyright John Wiley and Sons 2011.

#### 4.3. Fuel Cells

Fuel cells provide an efficient route for the conversion of chemically stored energy into electrical energy, and fuel cell electrocatalysts are critical to reduce overpotential losses due to hydrogen oxidation or oxygen reduction reactions at the anode and cathode [128,129]. Electrocatalysts should have high catalytic activity, large surface areas, high electrical conductivity, good corrosion resistance, and durability [128]. Generally, VACNTs have high conductivity, high corrosion resistance, and large surface areas with controllable aspect ratios, making them very suitable for catalyst support materials [130–132]. Recently, some VACNT–inorganic hybrids were developed to improve the performance of fuel cells [129]. In 2012, Dameron et al. used ALD to deposit uniform platinum (Pt) nanoparticles/films on functionalized multiwalled VACNTs using trimethyl(methylcyclopentadienyl)platinum (MeCpPtMe<sub>3</sub>) and O<sub>2</sub>, as shown in Figure 8 [129]. Before the deposition of Pt, the surfaces of the VACNTs were functionalized using the plasma of O<sub>2</sub>, which created new oxygen-incorporated nucleation sites that acted as chemical footholds for surface oxidation of the Pt precursors during ALD growth [129]. As a result, the surface functionalization apparently improved the uniformity of the Pt coating along the length of VACNTs within the aligned arrays and finally affected the performances of fuel cells toward the oxygen reduction reaction [129]. Therefore, the core-sheath-structured VACNT–inorganic hybrids are promising for use in fuel cells for the reduction of their overpotential losses.

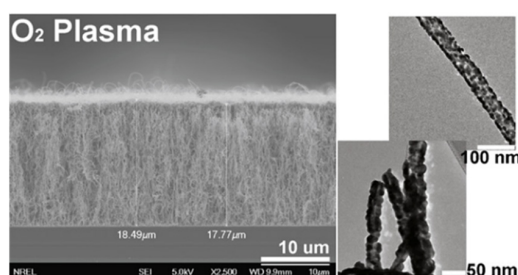


**Figure 8.** (Color online) SEM and TEM images of Pt deposition on the oxygen plasma-functionalized VACNTs [129]. Copyright Elsevier 2012.

#### 4.4. Sensors

For the detection and identification of target chemical and biological agents, sensors have been widely used in environmental monitoring, threat detection, and clinical diagnostics [133–137]. Generally, individual sensing units were set on a planar substrate, but two-dimensional (2D) structures severely limited access of target molecules to the sensing elements [138]. Currently, a nanoscale 3D architecture has also been developed for the fabrication of highly sensitive and rapid sensor responses [138]. In 2012, Zhao et al. used ALD to directly deposit  $\text{Al}_2\text{O}_3$  films on VACNTs for the fabrication of VACNT-based chemical sensors, and the  $\text{Al}_2\text{O}_3$  films prevented potential shortages between the inner and outer coax electrodes, as shown in Figure 9 [138]. The coaxial units were mechanically polished and allowed access to the p- $\text{Al}_2\text{O}_3$  for target molecules, which included the VACNTs, alumina coatings by ALD (a- $\text{Al}_2\text{O}_3$ ) and sputtering (p- $\text{Al}_2\text{O}_3$ ), and aluminum (Al) coating by sputtering, and were ultimately supported by SU8 polymers. From Figure 8, we can also see that the outer (Al) and inner (VACNTs) coax conductors formed nanocoaxial cables whose equivalent circuit was a resistor (R) and capacitor (C) connected in parallel [138]. VACNTs were connected to a bottom titanium (Ti) film to form electrode 1, and the outer Al coating formed electrode 2. In contrast to a- $\text{Al}_2\text{O}_3$ , p- $\text{Al}_2\text{O}_3$  could capture chemical molecules by chemiphysical adsorption, leading to changes in the sensor impedance as well as its components, R and C [138]. Compared with 2D planar structures, 3D structural sensors enabled rapid access of target molecules to the active sensing elements, and the dense array yielded a multiplicative effect on the signal amplitude [138]. Thus, the core-sheath-structured VACNT–inorganic hybrids are very suitable for the fabrication of sensors, and can largely improve their sensitivity.

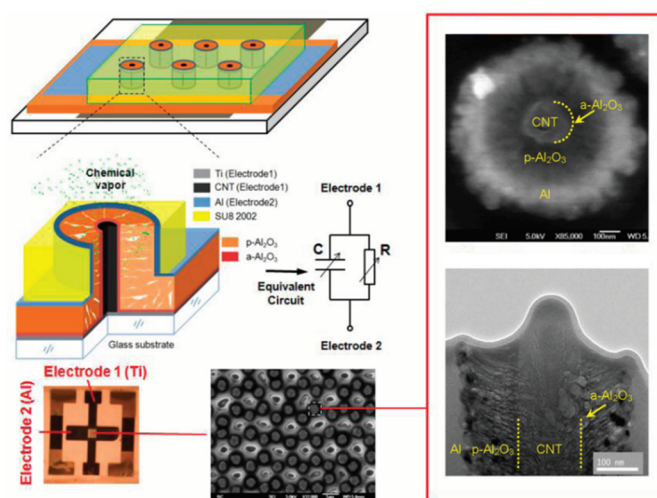


**Figure 9.** (Color online) The VACNT-based chemical sensor. Its structure is composed of VACNTs, ALD a- $\text{Al}_2\text{O}_3$ , sputtering p- $\text{Al}_2\text{O}_3$ , sputtering Al, and SU8 polymers, which are shown by SEM and TEM at low and high magnifications [138]. Copyright ACS Publication 2012.

## 5. Conclusions

ALD involves self-limited behavior, which can deposit uniform and conformal inorganic films on a high-aspect-ratio 3D structure with atomic scale precision. It is very suitable for the conformal deposition of catalysts for the growth of VACNTs on 3D structures and uniform coating of inorganic films on VACNTs to achieve core-sheath-structured VACNT–inorganic hybrids. Due to the complex topology and surface of VACNTs, it generally takes a long time to deposit uniform inorganic films on them, and occasionally, surface functionalization processes are also required to make reactive surface groups available, which could assist in chemisorbing the molecules and serve as nucleation sites for the subsequent deposition on VACNTs. For the core-sheath-structured VACNT–inorganic hybrids, they apparently enhance the charge storage capacity of supercapacitors, overall conversion

efficiency of solar cells, sensitivity of sensors, and reduce the overpotential losses of fuel cells. Due to the outstanding properties of VACNTs, the ALD-elaborated VACNT–inorganic hybrids showed interesting performances in many potential applications, such as supercapacitors, solar cells, fuel cells, and sensors.

**Author Contributions:** Conceptualization, G.-J.Y., H.-L.L., and Y.-Z.T.; validation, G.-J.Y., J.-F.X., and H.-H.L.; formal analysis, G.-J.Y., and J.F.X.; investigation, G.-J.Y., and J.-F.X.; resources, G.-J.Y. and J.-F.X.; data curation, G.-J.Y. and J.-F.X.; writing—original draft preparation, G.-J.Y., and J.F.X.; writing—review and editing, G.-J.Y., H.-L.L., and Y.-Z.T.; visualization, G.-J.Y. and J.-F.X.; supervision, G.-J.Y. and Y.-Z.T.; project administration, G.-J.Y. and Y.-Z.T.; funding acquisition, G.-J.Y. and Y.-Z.T.

**Funding:** This research was funded by the National Natural Science Foundation of China, grant number were 61704102 and 51861135105.

**Acknowledgments:** The authors thank Yong Zhang from the School of Automation and Mechanical Engineering, Shanghai University, for the useful discussions.

**Conflicts of Interest:** The authors declare no conflict of interest.

## References

1. Ren, Z.F.; Huang, Z.P.; Xu, J.W.; Wang, J.H.; Bush, P.; Siegal, M.P.; Provencio, P.N. Synthesis of large arrays of well-aligned carbon nanotubes on glass. *Science* **1998**, *282*, 1105–1107. [[CrossRef](#)] [[PubMed](#)]
2. Wei, B.Q.; Vajtai, R.; Jung, Y.; Ward, J.; Zhang, R.; Ramanath, G.; Ajayan, P.M. Organized assembly of carbon nanotubes. *Nature* **2002**, *416*, 495–496. [[CrossRef](#)] [[PubMed](#)]
3. Suhr, J.; Victor, P.; Ci, L.; Sreekala, S.; Zhang, X.; Nalamasu, O.; Ajayan, P.M. Fatigue resistance of aligned carbon nanotube arrays under cyclic compression. *Nat. Nanotechnol.* **2007**, *2*, 417–421. [[CrossRef](#)] [[PubMed](#)]
4. Qu, L.T.; Dai, L.M.; Stone, M.; Xia, Z.H.; Wang, Z.L. Carbon nanotube arrays with strong shear binding-on and easy normal lifting-off. *Science* **2008**, *322*, 238–242. [[CrossRef](#)] [[PubMed](#)]
5. Xiong, G.P.; He, P.G.; Lyu, Z.P.; Chen, T.F.; Huang, B.; Chen, L.; Fisher, T.S. Bioinspired leaves-on-branchlet hybrid carbon nanostructure for supercapacitors. *Nat. Commun.* **2018**, *9*, 790. [[CrossRef](#)]
6. Gupta, B.K.; Kedawat, G.; Gangwar, A.K.; Nagpal, K.; Kashyap, P.K.; Srivastava, S.; Singh, S.; Kumar, P.; Suryawanshi, S.R.; Seo, D.M.; et al. High-performance field emission device utilizing vertically aligned carbon nanotubes-based pillar architectures. *AIP Adv.* **2018**, *8*, 015117. [[CrossRef](#)]
7. Lin, P.H.; Sie, C.L.; Chen, C.A.; Chang, H.C.; Shih, Y.T.; Chang, H.Y.; Su, W.J.; Lee, K.Y. Field emission characteristics of the structure of vertically aligned carbon nanotube bundles. *Nanoscale Res. Lett.* **2015**, *10*, 297. [[CrossRef](#)]
8. Maschmann, M.R.; Dickinson, B.; Ehlert, G.J.; Baur, J.W. Force sensitive carbon nanotube arrays for biologically inspired airflow sensing. *Smart Mater. Struct.* **2012**, *21*, 094024. [[CrossRef](#)]
9. Yang, J.; Zhang, W.D.; Gunasekaran, S. An amperometric non-enzymatic glucose sensor by electrodepositing copper nanocubes onto vertically well-aligned multi-walled carbon nanotube arrays. *Biosens. Bioelectron.* **2010**, *26*, 279–284. [[CrossRef](#)]
10. Jiang, Y.Q.; Wang, P.B.; Zang, X.N.; Yang, Y.; Kozinda, A.; Lin, L.W. Uniformly embedded metal oxide nanoparticles in vertically aligned carbon nanotube forests as pseudocapacitor electrodes for enhanced energy storage. *Nano Lett.* **2013**, *13*, 3524–3530. [[CrossRef](#)]
11. Zhang, Q.C.; Wang, X.N.; Pan, Z.H.; Sun, J.; Zhao, J.X.; Zhang, J.; Zhang, C.X.; Tang, L.; Luo, J.; Song, B.; et al. Wrapping aligned carbon nanotube composite sheets around vanadium nitride nanowire arrays for asymmetric coaxial fiber-shaped supercapacitors with ultrahigh energy density. *Nano Lett.* **2017**, *17*, 2719–2726. [[CrossRef](#)] [[PubMed](#)]
12. Kaur, S.; Raravikar, N.; Helms, B.A.; Prasher, R.; Ogletree, D.F. Enhanced thermal transport at covalently functionalized carbon nanotube array interfaces. *Nat. Commun.* **2014**, *5*, 3082. [[CrossRef](#)] [[PubMed](#)]
13. Yao, Y.G.; Tey, J.N.; Li, Z.; Wei, J.; Bennett, K.; McNamara, A.; Joshi, Y.; Tan, R.L.S.; Ling, S.N.M.; Wong, C.P. High-quality vertically aligned carbon nanotubes for applications as thermal interface materials. *IEEE Trans. Compon. Packag. Manuf.* **2014**, *4*, 232–239. [[CrossRef](#)]
14. Baughman, R.H.; Zakhidov, A.A.; Heer, W.A.D. Carbon nanotubes—the route toward application. *Science* **2002**, *297*, 787–792. [[CrossRef](#)] [[PubMed](#)]

15. Wei, F.; Zhang, Q.; Qian, W.Z.; Xu, G.H.; Xiang, R.; Wen, Q.; Wang, Y.; Luo, G.H. Progress on aligned carbon nanotube arrays. *New Carbon Mater.* **2007**, *22*, 271–282.
16. Li, H.H.; Yuan, G.J.; Shan, B.; Zhang, X.X.; Ma, H.P.; Tian, Y.Z.; Lu, H.L.; Liu, J. Chemical vapor deposition of vertically aligned carbon nanotube arrays: Critical effects of oxide buffer layers. *Nanoscale Res. Lett.* **2019**, *14*, 106. [[CrossRef](#)] [[PubMed](#)]
17. Bekyarov, E.; Thostenson, E.T.; Yu, A.; Kim, H.; Gao, J.; Tang, J.; Hahn, H.T.; Chou, T.W.; Itkis, M.E.; Haddon, R.C. Multiscale Carbon nanotube–carbon fiber reinforcement for advanced epoxy composites. *Langmuir* **2007**, *23*, 3970–3974. [[CrossRef](#)]
18. Li, Y.; Huang, Z.; Huang, K.; Carnahan, D.; Xing, Y. Hybrid Li-air battery cathodes with sparse carbon nanotube arrays directly grown on carbon fiber papers. *Energy Environ. Sci.* **2013**, *6*, 3339–3345. [[CrossRef](#)]
19. Su, D.S.; Schlogl, R. Nanostructured carbon and carbon nanocomposites for electrochemical energy storage applications. *ChemSusChem* **2010**, *3*, 136–168. [[CrossRef](#)]
20. Su, D.S.; Chen, X.W.; Weinberg, G.; Hofmann, A.K.; Timpe, O.; Hamid, S.B.A.; Schlogl, R. Hierarchically structured carbon: Synthesis of carbon nanofibers nested inside or immobilized onto modified activated carbon. *Angew. Chem. Int. Ed.* **2005**, *44*, 5488–5492. [[CrossRef](#)]
21. Zhang, Q.; Huang, J.Q.; Zhao, M.Q.; Qian, W.Z.; Wang, Y.; Wei, F. Radial growth of vertically aligned carbon nanotube arrays from ethylene on ceramic spheres. *Carbon* **2008**, *46*, 1152–1158. [[CrossRef](#)]
22. Singh, C.; Shaffer, M.S.P.; Koziol, K.K.K.; Kinloch, I.A.; Windle, A.H. Towards the production of large-scale aligned carbon nanotubes. *Chem. Phys. Lett.* **2003**, *372*, 860–865. [[CrossRef](#)]
23. Xiang, R.; Luo, G.H.; Qian, W.Z.; Wang, Y.; Wei, F.; Li, Q. Large area growth of aligned CNT arrays on spheres: Towards large scale and continuous production. *Chem. Vapor Depos.* **2007**, *13*, 533–536. [[CrossRef](#)]
24. Ye, J.S.; Cui, H.F.; Liu, X.; Lim, T.M.; Zhang, W.D.; Sheu, F.S. Preparation and characterization of aligned carbon nanotube-ruthenium oxide nanocomposites for supercapacitors. *Small* **2005**, *5*, 560–565. [[CrossRef](#)] [[PubMed](#)]
25. Hsia, B.; Marschewski, J.; Wang, S.; In, J.B.; Carraro, C.; Poulikakos, D.; Grigoropoulos, C.P.; Maboudian, R. Highly flexible, all solid-state micro-supercapacitors from vertically aligned carbon nanotubes. *Nanotechnology* **2014**, *25*, 055401. [[CrossRef](#)]
26. Liu, J.W.; Kuo, Y.T.; Klabunde, K.J.; Rochford, C.; Wu, J.; Li, J. Novel dye-sensitized solar cell architecture using TiO<sub>2</sub>-coated vertically aligned carbon nanofiber arrays. *ACS Appl. Mater. Interfaces* **2009**, *1*, 1645–1649. [[CrossRef](#)]
27. Kilic, B.; Turkdogan, S.; Astam, A.; Ozer, O.C.; Asgin, M.; Cebeci, H.; Urk, D.; Mucur, S.P. Preparation of carbon nanotube/TiO<sub>2</sub> mesoporous hybrid photoanode with iron pyrite (FeS<sub>2</sub>) thin films counter electrodes for dye-sensitized solar cell. *Sci. Rep.* **2016**, *6*, 27052. [[CrossRef](#)]
28. Tian, Z.Q.; Lim, S.H.; Poh, C.K.; Tang, Z.; Xia, Z.T.; Luo, Z.Q.; Shen, P.K.; Chua, D.; Feng, Y.P.; Shen, Z.X.; et al. A highly order-structured membrane electrode assembly with vertically aligned carbon nanotubes for ultra-low Pt loading PEM fuel cells. *Adv. Energy Mater.* **2011**, *1*, 1205–1214. [[CrossRef](#)]
29. Zhang, W.M.; Minett, A.I.; Gao, M.; Zhao, J.; Razal, J.M.; Wallace, G.G.; Romeo, T.; Chen, J. Integrated high-efficiency Pt/carbon nanotube arrays for PEM fuel cells. *Adv. Energy Mater.* **2011**, *1*, 671–677. [[CrossRef](#)]
30. Yick, S.; Han, Z.J.; Ostrikov, K. Atmospheric microplasma-functionalized 3D microfluidic strips within dense carbon nanotube arrays confine Au nanodots for SERS sensing. *Chem. Commun.* **2013**, *49*, 2861–2863. [[CrossRef](#)]
31. Stano, K.L.; Carroll, M.; Padbury, R.; McCord, M.; Jur, J.S.; Bradford, P.D. Conformal atomic layer deposition of alumina on millimeter tall, vertically-aligned carbon nanotube arrays. *ACS Appl. Mater. Interfaces* **2014**, *6*, 19135–19143. [[CrossRef](#)] [[PubMed](#)]
32. Yazdani, N.; Chawla, V.; Edwards, E.; Wood, V.; Park, H.G.; Utke, I. Modeling and optimization of atomic layer deposition processes on vertically aligned carbon nanotubes. *Beilstein J. Nanotechnol.* **2014**, *5*, 234–244. [[CrossRef](#)] [[PubMed](#)]
33. Shimizu, H.; Sakoda, K.; Momose, T.; Koshi, M.; Shimogaki, Y. Hot-wire assisted atomic layer deposition of a high quality cobalt film using cobaltocene: Elementary reaction analysis on NH<sub>x</sub> radical formation. *J. Vac. Sci. Technol. A* **2012**, *20*, 01A144. [[CrossRef](#)]
34. Gordon, R.G.; Hausmann, D.; Kim, E.; Shepard, J. A kinetic model for step coverage by atomic layer deposition in narrow holes or trenches. *Chem. Vapor Depos.* **2003**, *9*, 73–78. [[CrossRef](#)]

35. Knez, M.; Nielsh, K.; Niinisto, L. Synthesis and surface engineering of complex nanostructures by atomic layer deposition. *Adv. Mater.* **2007**, *19*, 3425–3438. [[CrossRef](#)]
36. Detavernier, C.; Dendooven, J.; Sree, S.P.; Ludwig, K.F.; Martens, J.A. Tailoring nanoporous materials by atomic layer deposition. *Chem. Soc. Rev.* **2011**, *40*, 5242–5253. [[CrossRef](#)]
37. Zazpe, R.; Knaut, M.; Sopha, H.; Hromadko, L.; Albert, M.; Prikryl, J.; Gartnerova, V.; Bartha, J.W.; Macak, J.M. Atomic layer deposition for coating high aspect ratio TiO<sub>2</sub> nanotube layers. *Langmuir* **2016**, *32*, 10551–10558. [[CrossRef](#)]
38. Weber, M.; Julbe, A.; Ayril, A.; Miele, P.; Bechelany, M. Atomic layer deposition for membranes: Basics, challenges, and opportunities. *Chem. Mater.* **2018**, *30*, 7368–7390. [[CrossRef](#)]
39. Graniel, O.; Weber, M.; Balme, S.; Miele, P.; Bechelany, M. Atomic layer deposition for biosensing applications. *Biosens. Bioelectron.* **2018**, *122*, 147–159. [[CrossRef](#)]
40. Marichy, C.; Pinna, N. Carbon-nanostructures coated/decorated by atomic layer deposition: Growth and applications. *Coord. Chem. Rev.* **2013**, *257*, 3232–3253. [[CrossRef](#)]
41. Kim, J.Y.; Kim, J.H.; Ahn, J.H.; Park, P.K.; Kang, S.W. Applicability of step-coverage modeling to TiO<sub>2</sub> thin films in atomic layer deposition. *J. Electrochem. Soc.* **2007**, *154*, H1008–H1013. [[CrossRef](#)]
42. Kim, Y.S.; Yun, S.J. Nanolaminated Al<sub>2</sub>O<sub>3</sub>-TiO<sub>2</sub> thin films grown by atomic layer deposition. *J. Cryst. Growth* **2005**, *274*, 585–593. [[CrossRef](#)]
43. George, S.M. Atomic layer deposition: An overview. *Chem. Rev.* **2010**, *110*, 111–131. [[CrossRef](#)] [[PubMed](#)]
44. Miikkulainen, V.; Leskela, M.; Ritala, M.; Puurunen, R.L. Crystallinity of inorganic films grown by atomic layer deposition: Overview and general trends. *J. Appl. Phys.* **2013**, *113*, 021301. [[CrossRef](#)]
45. Johnson, R.W.; Hultqvist, A.; Bent, S.F. A brief review of atomic layer deposition: From fundamentals to applications. *Mater. Today* **2014**, *17*, 236–246. [[CrossRef](#)]
46. Ponraj, J.S.; Attolini, G.; Bosi, M. Review on atomic layer deposition and applications of oxide thin films. *Crit. Rev. Solid State* **2013**, *38*, 203–233. [[CrossRef](#)]
47. Puurunen, R.L.; Root, A.; Haukka, S.; Iiskola, E.I.; Lindblad, M.; Krause, A.O.I. IR and NMR study of the chemisorptions of ammonia on trimethylaluminum-modified silica. *J. Phys. Chem. B* **2000**, *104*, 6599–6609. [[CrossRef](#)]
48. Puurunen, R.L. Growth per cycle in atomic layer deposition: Real application examples of a theoretical model. *Chem. Vap. Depos.* **2003**, *9*, 327–332. [[CrossRef](#)]
49. Muneshwar, T.; Cadien, K. AxBAxB ... pulsed atomic layer deposition: Numerical growth model and experiments. *J. Appl. Phys.* **2016**, *119*, 085306. [[CrossRef](#)]
50. Nazarov, D.V.; Bobrysheva, N.P.; Osmolovskaya, O.M.; Osmolovsky, M.G.; Smirnov, V.M. Atomic layer deposition of TiN dioxide nanofilms: A review. *Rev. Adv. Mater. Sci.* **2015**, *40*, 262–275.
51. Austin, D.Z.; Jenkins, M.A.; Allman, D.; Hose, S.; Price, D.; Dezelah, C.L.; Conley, J.F. Atomic layer deposition of ruthenium and ruthenium oxide using a zero-oxidation state precursor. *Chem. Mater.* **2017**, *29*, 1107–1115. [[CrossRef](#)]
52. Parsons, G.N.; George, S.M.; Knez, M.; Editors, G. Progress and future directions for atomic layer deposition and ALD-based chemistry. *MRS Bull.* **2011**, *36*, 865–871. [[CrossRef](#)]
53. Niinisto, J.; Mantymaki, M.; Kukli, K.; Costelle, L.; Puukilainen, E.; Ritala, M.; Leskela, M.J. Growth and phase stabilization of HfO<sub>2</sub> thin films by ALD using novel precursors. *J. Cryst. Growth* **2010**, *312*, 245–249.
54. Putkonen, M.; Sajavaara, T.; Niinisto, L.; Keinonen, J. Analysis of ALD-processed thin films by ion-beam techniques. *Anal. Bioanal. Chem.* **2005**, *382*, 1792–1799. [[CrossRef](#)]
55. Puurunen, R.L.; Root, A.; Sarv, P.; Viitanen, M.M.; Brongersma, H.H.; Lindblad, M.; Krause, A.O.I. Growth of aluminum nitride on porous alumina and silica through separate saturated gas-solid reactions of trimethylaluminum and ammonia. *Chem. Mater.* **2002**, *14*, 720–729. [[CrossRef](#)]
56. Puurunen, R.L.; Airaksinen, S.M.K.; Krause, A.O.I. Chromium (III) supported on aluminum-nitride-surfaced alumina: Characteristics and dehydrogenation activity. *J. Catal.* **2003**, *213*, 281–290. [[CrossRef](#)]
57. Zhong, J.; Wang, J.; Huang, G.S.; Yuan, G.L.; Mei, Y.F. Effect of physisorption and chemisorptions of water on resonant modes of rolled-up tubular microcavities. *Nanoscale Res. Lett.* **2013**, *8*, 531. [[CrossRef](#)]
58. Jeong, S.J.; Kim, H.W.; Heo, J.; Lee, M.H.; Song, H.J.; Ku, J.; Lee, Y.; Cho, Y.; Jeon, W.; Suh, H.; et al. Physisorbed-precursor-assisted atomic layer deposition of reliable ultrathin dielectric films on inert graphene surfaces for low-power electronics. *2D Mater.* **2016**, *3*, 035327. [[CrossRef](#)]

59. Teng, H.; Hsieh, C.T. Activation energy for oxygen chemisorptions on carbon at low temperatures. *Ind. Eng. Chem. Res.* **1999**, *38*, 292–297. [[CrossRef](#)]
60. Sudan, P.; Zuttel, A.; Mauron, P.; Emmenegger, C.; Wenger, P.; Schlapbach, L. Physisorption of hydrogen in single-walled carbon nanotubes. *Carbon* **2003**, *41*, 2377–2383. [[CrossRef](#)]
61. Ritala, M.; Leskela, M.; Rauhala, E.; Haussalo, P. Atomic layer epitaxy growth of TiN thin films. *J. Electrochem. Soc.* **1995**, *142*, 2731–2737. [[CrossRef](#)]
62. Becker, J.B.; Suh, S.; Wang, S.L.; Gorden, R.G. Highly conformal thin films of tungsten nitride prepared by atomic layer deposition from a novel precursor. *Chem. Mater.* **2003**, *15*, 2969–2976. [[CrossRef](#)]
63. Ott, A.W.; Klaus, J.W.; Johnson, J.M.; George, S.M. Al<sub>2</sub>O<sub>3</sub> thin film growth on Si(100) using binary reaction sequence chemistry. *Thin Solid Films* **1997**, *292*, 135–144. [[CrossRef](#)]
64. Groner, M.D.; Fabreguette, F.H.; Elam, J.W.; George, S.M. Low-temperature Al<sub>2</sub>O<sub>3</sub> atomic layer deposition. *Chem. Mater.* **2004**, *16*, 639–645. [[CrossRef](#)]
65. Kim, S.; Lee, S.; Ham, S.Y.; Ko, D.H.; Shin, S.; Jin, Z.Y.; Min, Y.S. A kinetic study of ZnO atomic layer deposition: Effect of surface hydroxyl concentration and steric hindrance. *Appl. Surf. Sci.* **2019**, *469*, 804–810. [[CrossRef](#)]
66. Leskela, M.; Ritala, M. Atomic layer deposition (ALD): From precursors to thin film structures. *Thin Solid Films* **2002**, *409*, 138–146. [[CrossRef](#)]
67. Ajayan, P.M.; Ebbesen, T.W.; Ichihashi, T.; Iijima, S.; Tanigaki, K.; Hiura, H. Opening carbon nanotubes with oxygen and implications for filling. *Nature* **1993**, *362*, 522–525. [[CrossRef](#)]
68. Penza, M.; Rossi, R.; Alvisi, M.; Serra, E. Metal-modified and vertically aligned carbon nanotube sensors arrays for landfill gas monitoring applications. *Nanotechnology* **2010**, *21*, 105501. [[CrossRef](#)]
69. Kong, J.; Cassell, A.M.; Dai, H. Chemical vapor deposition of methane for single-walled carbon nanotubes. *Chem. Phys. Lett.* **1998**, *292*, 567–574. [[CrossRef](#)]
70. Wal, R.L.V.; Ticich, T.M. Comparative flame and furnace synthesis of single-walled carbon nanotubes. *Chem. Phys. Lett.* **2001**, *336*, 24–32.
71. Laplaze, D.; Bernier, P.; Maser, W.K.; Flamant, G.; Guillard, T.; Loiseau, A. Carbon nanotubes: The solar approach. *Carbon* **1998**, *36*, 685–688. [[CrossRef](#)]
72. De, I.A.T.; Garnier, M.G.; Seo, J.K.; Oelhafen, P.; Thommen, V.; Mathys, D. The influence of catalyst chemical state and morphology on carbon nanotube growth. *J. Phys. Chem. B* **2004**, *108*, 7728–7734.
73. Fiawoo, M.F.C.; Bonnot, A.M.; Amara, H.; Bichara, C.; Thibault-Penisson, J.; Loiseau, A. Evidence of correlation between catalyst particles and the single-wall carbon nanotube diameter: A first step towards chirality control. *Phys. Rev. Lett.* **2012**, *108*, 195503. [[CrossRef](#)] [[PubMed](#)]
74. Li, H.H.; Yuan, G.J.; Shan, B.; Zhang, X.X.; Ma, H.P.; Tian, Y.Z.; Lu, H.L.; Liu, J. Atomic layer deposition of buffer layers for the growth of vertically aligned carbon nanotube arrays. *Nanoscale Res. Lett.* **2019**, *14*, 119. [[CrossRef](#)] [[PubMed](#)]
75. Thissen, N.F.W.; Verheijen, M.A.; Houben, R.G.; Marel, C.V.D.; Kessels, W.M.M.; Bol, A.A. Synthesis of single-walled carbon nanotubes from atomic-layer-deposited Co<sub>3</sub>O<sub>4</sub> and Co<sub>3</sub>O<sub>4</sub>/Fe<sub>2</sub>O<sub>3</sub> catalyst films. *Carbon* **2017**, *121*, 389–398. [[CrossRef](#)]
76. Yoon, Y.J.; Bae, J.C.; Baik, H.K.; Cho, S.; Lee, S.J.; Song, K.M.; Myung, N.S. Growth control of single and multi-walled carbon nanotubes by thin film catalyst. *Chem. Phys. Lett.* **2002**, *366*, 109–114. [[CrossRef](#)]
77. Esconjauregui, S.; Fouquet, M.; Bayer, B.C.; Ducati, C.; Smajda, R.; Hofmann, S.; Robertson, J. Growth of ultrahigh density vertically aligned carbon nanotube forests for interconnects. *ACS Nano* **2010**, *4*, 7431–7436. [[CrossRef](#)]
78. Tang, L.; Zhang, Q.C.; Li, C.W.; Wang, X.N.; Zhang, K.; Xu, Y.C.; Li, T.T.; Fang, J.H.; Yao, Y.G. Atomic layer deposition of Al<sub>2</sub>O<sub>3</sub> catalysts for narrow diameter distributed single-walled carbon nanotube arrays growth. *Carbon* **2017**, *114*, 224–229. [[CrossRef](#)]
79. Liu, H.; Zhang, Y.; Arato, D.; Li, R.Y.; Merel, P.; Sun, X.L. Aligned multi-walled carbon nanotubes on different substrates by floating catalyst chemical vapor deposition: Critical effects of buffer layer. *Surf. Coat. Technol.* **2008**, *202*, 4114–4120. [[CrossRef](#)]
80. Zhou, K.; Huang, J.Q.; Zhang, Q.; Wei, F. Multi-directional growth of aligned carbon nanotubes over catalyst film prepared by atomic layer deposition. *Nanoscale Res. Lett.* **2010**, *5*, 1555–1560. [[CrossRef](#)]

81. Chen, B.A.; Zhang, C.; Esconjauregui, S.; Xie, R.S.; Zhong, G.F.; Bhardwaj, S.; Cepek, C.; Robertson, J. Carbon nanotube forests growth using catalysts from atomic layer deposition. *J. Appl. Phys.* **2014**, *115*, 144303. [[CrossRef](#)]
82. Eder, D. Carbon nanotube-inorganic hybrids. *Chem. Rev.* **2010**, *110*, 1348–1385. [[CrossRef](#)] [[PubMed](#)]
83. Li, X.L.; Li, C.; Zhang, Y.; Chu, D.P.; Milne, W.I.; Fan, H.J. Atomic layer deposition of ZnO on multi-walled carbon nanotubes and its use for synthesis of CNT-ZnO heterostructures. *Nanoscale Res. Lett.* **2010**, *5*, 1836–1840. [[CrossRef](#)] [[PubMed](#)]
84. Haremza, J.M.; Hahn, M.A.; Krauss, T.D.; Chen, S.; Calcines, J. Attachment of single CdSe nanocrystals to individual single-walled carbon nanotubes. *Nano Lett.* **2002**, *2*, 1253–1258. [[CrossRef](#)]
85. Aarik, J.; Aidla, A.; Mandar, H.; Uustare, T. Atomic layer deposition of titanium dioxide from TiCl<sub>4</sub> and H<sub>2</sub>O: Investigation of growth mechanism. *Appl. Surf. Sci.* **2001**, *172*, 148–158. [[CrossRef](#)]
86. Aarik, J.; Aidla, A.; Uustare, T.; Ritala, M.; Leskela, M. Titanium isopropoxide as a precursor for atomic layer deposition: Characterization of titanium dioxide growth process. *Appl. Surf. Sci.* **2000**, *161*, 385–395. [[CrossRef](#)]
87. Herrmann, C.F.; Fabreguette, F.H.; Finch, D.S.; Geiss, R.; George, S.M. Multilayer and functional coatings on carbon nanotubes using atomic layer deposition. *Appl. Phys. Lett.* **2005**, *87*, 123110. [[CrossRef](#)]
88. Lu, Y.R.; Bangsaruntip, S.; Wang, X.R.; Zhang, L.; Nishi, Y.; Dai, H.J. DNA functionalization of carbon nanotubes for ultrathin atomic layer deposition of high k dielectrics for nanotube transistors with 60 mV/decade switching. *J. Am. Chem. Soc.* **2006**, *128*, 3518–3519. [[CrossRef](#)]
89. Wang, X.R.; Tabakman, S.; Dai, H.J. Atomic layer deposition of metal oxides on pristine and functionalized graphene. *J. Am. Chem. Soc.* **2008**, *130*, 8152–8153. [[CrossRef](#)]
90. Xuan, Y.; Wu, Y.Q.; Shen, T.; Qi, M.; Capano, M.A.; Cooper, J.A.; Ye, P.D. Atomic-layer-deposited nanostructures for graphene-based nanoelectronics. *Appl. Phys. Lett.* **2008**, *92*, 013101. [[CrossRef](#)]
91. Cavanagh, A.S.; Wilson, C.A.; Weimer, A.W.; George, S.M. Atomic layer deposition on gram quantities of multi-walled carbon nanotubes. *Nanotechnology* **2009**, *20*, 255602. [[CrossRef](#)] [[PubMed](#)]
92. Lim, J.W.; Park, H.S.; Kang, S.W. Kinetic modeling of film growth rate in atomic layer deposition. *J. Appl. Phys.* **2001**, *148*, C403–C408. [[CrossRef](#)]
93. Yazdani, N.; Bozyigit, D.; Utke, I.; Buchheim, J.; Youn, S.K.; Patscheider, J.; Wood, V.; Park, H.G. Enhanced charge transport kinetics in anisotropic, stratified photoanodes. *ACS Appl. Mater. Interfaces* **2014**, *6*, 1389–1393. [[CrossRef](#)] [[PubMed](#)]
94. Min, Y.S.; Lee, I.H.; Lee, Y.H.; Hwang, C.S. Botryoidal growth of crystalline ZnO nanoparticles on a forest of single-walled carbon nanotubes by atomic layer deposition. *CrystEngComm* **2011**, *13*, 3451–3454. [[CrossRef](#)]
95. Lee, J.S.; Min, B.; Cho, K.; Kim, S.; Park, J.; Lee, Y.T.; Kim, N.S.; Lee, M.S.; Park, S.O.; Moon, J.T. Al<sub>2</sub>O<sub>3</sub> nanotubes and nanorods fabricated by coating and filling of carbon nanotubes with atomic-layer deposition. *J. Cryst. Growth* **2003**, *254*, 443–448. [[CrossRef](#)]
96. Kim, D.S.; Lee, S.M.; Scholz, R.; Knez, M.; Gosele, U.; Fallert, J.; Kalt, H.; Zacharias, M. Synthesis and optical properties of ZnO and carbon nanotube based coaxial heterostructures. *Appl. Phys. Lett.* **2008**, *93*, 103108. [[CrossRef](#)]
97. Lahiri, I.; Oh, S.M.; Hwang, J.Y.; Kang, C.; Choi, M.; Jeon, H.; Banerjee, R.; Sun, Y.K.; Choi, W. Ultrathin alumina-coated carbon nanotubes as an anode for high capacity Li-ion batteries. *J. Mater. Chem.* **2011**, *21*, 13621–13626. [[CrossRef](#)]
98. Farmer, D.B.; Gordon, R.G. ALD of high-k dielectrics on suspended functionalized SWNTs. *Electrochem. Solid State Lett.* **2005**, *8*, G89–G91. [[CrossRef](#)]
99. Zhan, G.D.; Du, X.H.; King, D.M.; Hakim, L.F.; Liang, X.H.; McCormick, J.A.; Weimer, A.W. Atomic layer deposition on bulk quantities of surfactant-modified single-walled carbon nanotubes. *J. Am. Ceram. Soc.* **2008**, *91*, 831–835. [[CrossRef](#)]
100. Liyanage, L.S.; Cott, D.J.; Delabie, A.; Elshocht, S.V.; Bao, Z.N.; Wong, H.S.P. Atomic layer deposition of high-k dielectrics on single-walled carbon nanotubes: A Raman study. *Nanotechnology* **2013**, *24*, 245703. [[CrossRef](#)]
101. Li, M.Y.; Zu, M.; Yu, J.S.; Cheng, H.F.; Li, Q.W.; Li, B. Controllable synthesis of core-sheath structured aligned carbon nanotube/titanium dioxide hybrid fibers by atomic layer deposition. *Carbon* **2017**, *123*, 151–157. [[CrossRef](#)]

102. Boukhalfa, S.; Evanoff, K.; Yushin, G. Atomic layer deposition of vanadium oxide on carbon nanotubes for high-power supercapacitor electrodes. *Energy Environ. Sci.* **2012**, *5*, 6872–6879. [[CrossRef](#)]
103. Zhang, Y.; Guerra-Nunez, C.; Utke, I.; Michler, J.; Rossell, M.D.; Erni, R. Understanding and controlling nucleation and growth of TiO<sub>2</sub> deposited on multiwalled carbon nanotubes by atomic layer deposition. *J. Phys. Chem. C* **2015**, *119*, 3379–3387. [[CrossRef](#)]
104. Fiorentino, G.; Vollebregt, S.; Tichelaar, F.D.; Ishihara, R.; Sarro, P.M. Impact of the atomic layer deposition precursors diffusion on solid-state carbon nanotube based supercapacitors performances. *Nanotechnology* **2015**, *26*, 064002. [[CrossRef](#)] [[PubMed](#)]
105. Simon, P.; Gogotsi, Y. Materials for electrochemical capacitors. *Nat. Mater.* **2008**, *7*, 845–854. [[CrossRef](#)] [[PubMed](#)]
106. Yang, Z.G.; Zhang, J.L.; Meyer, M.K.; Lu, X.C.; Choi, D.; Lemmon, J.P.; Liu, J.G. Electrochemical energy storage for green grid. *Chem. Rev.* **2011**, *111*, 3577–3613. [[CrossRef](#)]
107. Sharma, P.; Bhatti, T.S. A review on electrochemical double-layer capacitors. *Energy Convers. Manag.* **2010**, *51*, 2901–2912. [[CrossRef](#)]
108. Jiang, Y.; Lin, L. A two-stage, self-aligned vertical densification process for as-grown CNT forests in supercapacitor applications. *Sens. Actuators A Phys.* **2012**, *188*, 261–267. [[CrossRef](#)]
109. Jiang, Y.; Kozinda, A.; Lin, L. Flexible energy storage devices based on carbon nanotube forests with built-in metal electrodes. *Sens. Actuators A Phys.* **2013**, *195*, 224–230. [[CrossRef](#)]
110. Futaba, D.N.; Hata, K.; Yamada, T.; Hiraoka, T.; Hayamizu, Y.; Kakudate, Y.; Tanaike, O. Shape-engineerable and highly densely packed single-walled carbon nanotubes and their application as super-capacitor electrodes. *Nat. Mater.* **2006**, *5*, 987–994. [[CrossRef](#)]
111. Turano, S.P.; Ready, W.J. Chemical vapor deposition synthesis of self-aligned carbon nanotube arrays. *J. Electron. Mater.* **2006**, *35*, 192–194. [[CrossRef](#)]
112. Reit, R.; Nguyen, J.; Ready, W.J. Growth time performance dependence of vertically aligned carbon nanotube supercapacitors grown on aluminum substrates. *Electrochim. Acta* **2013**, *91*, 96–100. [[CrossRef](#)]
113. Kao, E.; Yang, C.; Warren, R.; Kozinda, A.; Lin, L.W. ALD titanium nitride on vertically aligned carbon nanotube forests for electrochemical supercapacitors. *Sens. Actuators A Phys.* **2016**, *240*, 160–166. [[CrossRef](#)]
114. Pint, C.L.; Nicholas, N.W.; Xu, S.; Sun, Z.Z.; Tour, J.M.; Schmidt, H.K.; Gordon, R.G.; Hauge, R.H. Three dimensional solid-state supercapacitors from aligned single-walled carbon nanotube array templates. *Carbon* **2011**, *49*, 4890–4897. [[CrossRef](#)]
115. Fisher, R.A.; Watt, M.R.; Konjeti, R.; Ready, W.J. Atomic layer deposition of titanium oxide for pseudocapacitive functionalization of vertically-aligned carbon nanotube supercapacitor electrodes. *ECS J. Solid State* **2015**, *4*, M1–M5. [[CrossRef](#)]
116. Warren, R.; Sammoura, F.; Tounsi, F.; Sanghadasa, M.; Lin, L.W. Highly active ruthenium oxide coating via ALD and electrochemical activation in supercapacitor applications. *J. Mater. Chem. A* **2015**, *3*, 15568–15575. [[CrossRef](#)]
117. Fan, Z.Y.; Razavi, H.; Do, J.W.; Moriwaki, A.; Ergen, O.; Chueh, Y.L.; Leu, P.W.; Ho, J.C.; Takahashi, T.; Reichertz, L.A.; et al. Three-dimensional nanopillar-array photovoltaics on low-cost and flexible substrates. *Nat. Mater.* **2009**, *8*, 648–653. [[CrossRef](#)]
118. Kamat, P.V. Meeting the clean energy demand: Nanostructure architectures for solar energy conversion. *J. Phys. Chem. C* **2007**, *111*, 2834–2860. [[CrossRef](#)]
119. Atwater, H.A.; Polman, A. Plasmonics for improved photovoltaic devices. *Nat. Mater.* **2010**, *9*, 205–213. [[CrossRef](#)]
120. Fan, Z.Y.; Kapadia, R.; Leu, P.W.; Zhang, X.B.; Chueh, Y.L.; Takei, K.; Yu, K.; Jamshidi, A.; Rathore, A.A.; Ruebusch, D.J.; et al. Ordered arrays of dual-diameter nanopillars for maximized optical absorption. *Nano Lett.* **2010**, *10*, 3823–3827. [[CrossRef](#)]
121. Huang, Y.F.; Chattopadhyay, S.; Jen, Y.J.; Peng, C.Y.; Liu, T.A.; Hsu, Y.K.; Pan, C.L.; Lo, H.C.; Hsu, C.H.; Chang, Y.H.; et al. Improved broadband and quasi-omnidirectional anti-reflection properties with biomimetic silicon nanostructures. *Nat. Nanotechnol.* **2007**, *2*, 770–774. [[CrossRef](#)] [[PubMed](#)]
122. Kapadia, R.; Fan, Z.Y.; Javery, A. Design constraints and guidelines for CdS/SdTe nanopillar based photovoltaics. *Appl. Phys. Lett.* **2010**, *96*, 103116. [[CrossRef](#)]
123. Lin, Y.J.; Yuan, G.B.; Liu, R.; Zhou, S.; Sheehan, S.W.; Wang, D.W. Semiconductor nanostructure-based photoelectrochemical water splitting: A brief review. *Chem. Phys. Lett.* **2011**, *507*, 209–215. [[CrossRef](#)]

124. Avouris, P.; Chen, Z.; Perebeinos, V. Carbon-based electronics. *Nat. Nanotechnol.* **2007**, *2*, 605–615. [[CrossRef](#)]
125. Rodriguez-Reinoso, F. The role of carbon materials in heterogeneous catalysis. *Carbon* **1998**, *36*, 159–175. [[CrossRef](#)]
126. Pint, C.L.; Takei, K.; Kapadia, R.; Zheng, M.; Ford, A.C.; Zhang, J.J.; Jamshidi, A.; Bardhan, R.; Urban, J.J.; Wu, M.; et al. Rationally designed, three-dimensional carbon nanotube back-contacts for efficient solar devices. *Adv. Energy Mater.* **2011**, *1*, 1040–1045. [[CrossRef](#)]
127. Yun, D.J.; Ra, H.; Kim, J.M.; Oh, E.; Lee, J.; Jeong, M.H.; Jeong, Y.J.; Yang, H.; Jang, J. Multi-walled carbon nanotube forests covered with atomic-layer-deposited ruthenium layers for high-performance counter electrodes of dye-sensitized solar cells. *Org. Electron.* **2019**, *65*, 349–356. [[CrossRef](#)]
128. Wang, Y.; Chen, K.S.; Mishler, J.; Cho, S.C.; Adroher, X.C. A review of polymer electrolyte membrane fuel cells: Technology, applications, and needs on fundamental research. *Appl. Energy* **2011**, *88*, 981–1007. [[CrossRef](#)]
129. Dameron, A.A.; Pylypenko, S.; Bult, J.B.; Neyerlin, K.C.; Engtrakul, C.; Bochert, C.; Leong, G.J.; Frisco, S.L.; Simpson, L.; Dinh, H.N.; et al. Aligned carbon nanotube array functionalization for enhanced atomic layer deposition of platinum electrocatalysts. *Appl. Surf. Sci.* **2012**, *258*, 5212–5221. [[CrossRef](#)]
130. Hu, X.G.; Dong, S.J. Metal nanomaterials and carbon nanotubes-synthesis, functionalization and potential applications towards electrochemistry. *J. Mater. Chem.* **2008**, *18*, 1279–1295. [[CrossRef](#)]
131. Zhang, W.M.; Sherrell, P.; Minett, A.I.; Razal, J.M.; Chen, J. Carbon nanotube architectures as catalyst supports for proton exchange membrane fuel cells. *Energy Environ. Sci.* **2010**, *3*, 1286–1293. [[CrossRef](#)]
132. Li, W.; Zie, S.; Qian, X.; Chang, L.; Zou, B.; Zhou, W.; Zhou, R.; Wang, G. Large-scale synthesis of aligned carbon nanotubes. *Science* **1996**, *274*, 1701–1703. [[CrossRef](#)] [[PubMed](#)]
133. Fan, F.R.F.; Bard, A.J. Electrochemical detection of single molecules. *Science* **1995**, *267*, 871–874. [[CrossRef](#)] [[PubMed](#)]
134. Chen, P.; Gu, J.; Brandin, E.; Kim, Y.R.; Wang, Q.; Branton, D. Probing single DNA molecule transport using fabricated nanopores. *Nano Lett.* **2004**, *4*, 2293–2298. [[CrossRef](#)]
135. Shekhawat, G.; Tark, S.H.; Dravid, V.P. Mosfet-embedded microcantilevers for measuring deflection in biomolecular sensors. *Science* **2006**, *311*, 1592–1595. [[CrossRef](#)]
136. Armani, A.M.; Kulkarni, R.P.; Fraser, S.E.; Flagan, R.C.; Vahala, K.J. Label-free, single-molecule detection with optical microcavities. *Science* **2007**, *317*, 783–787. [[CrossRef](#)]
137. Snow, E.S.; Perkins, F.K.; Houser, E.J.; Badescu, S.C.; Reinecke, T.L. Chemical detection with a single-walled carbon nanotube capacitor. *Science* **2005**, *307*, 1942–1945. [[CrossRef](#)]
138. Zhao, H.Z.; Rizal, B.; McMahon, G.; Wang, H.Z.; Dhakal, P.; Kirkpatrick, T.; Ren, Z.F.; Chiles, T.C.; Naughton, M.J.; Cai, D. Ultrasensitive chemical detection using a nanocoax sensor. *ACS Nano* **2012**, *6*, 3171–3178. [[CrossRef](#)]

